Temperature-dependent elasticity of single crystalline graphite

Franck Polewczyk, Jean-Marc Leyssale, Paul Lafourcade

Temperature-dependent elasticity of single crystalline graphite

Franck Polewczyk[a,b,c], Jean-Marc Leyssale[c], Paul Lafourcade[a,b,*]

[a] *CEA DAM DIF, 91297 Arpajon, France*
[b] *University of Paris-Saclay, LCME, 91280 Bruyères-le-Châtel, France*
[c] *University of Bordeaux, CNRS, Bordeaux INP, ISM, UMR 5255, F-33400 Talence, France*

Abstract

Despite its relevance in many high temperature processes, the elastic behavior of single crystalline graphite is so far entirely undocumented away from room temperature conditions. In this work we present a molecular dynamics investigation of graphite's second order elastic tensor dependence on temperature from 300 to 4000 K, using a series of popular interatomic potentials for carbon. Data and analytic expressions are presented for the elastic tensor under the two limiting situations known as isothermal, or quasi-static, and adiabatic deformation conditions, prevailing in the limits of slow and large deformation rates, respectively. Independently from the potential, we identify a strong non-linearity of elastic constants with respect to temperature. We show that despite conserving an important elastic anisotropy whatever the temperature, the latter is being reduced by a factor of ~ 5 when increasing temperature up to 4000 K. Also, we show that elastic anisotropy is about 20 times larger under isothermal conditions than under adiabatic conditions. Finally, we investigate the dynamics of the adiabatic to isothermal stress relaxations occurring right after ultra fast deformations such as those encountered under shock loading, showing that the relevant time and length scales are of the order of a few ps and nm, respectively, for deformations around a percent.

*Corresponding author
Email address: paul.lafourcade@cea.fr (Paul Lafourcade)

1. Introduction

When considering structural elements for devices experiencing ultra-high temperatures (UHT), like for instance thermal protection systems for atmospheric re-entry [1], involving temperatures in the 3000-4000 K range, very few materials are available [2]. Carbon based materials, and especially carbon/carbon (C/C) composites, combining high melting temperature, stiffness, strength and thermal conductivity, as well as low weight, are thus generally selected [3, 4]. However, despite numerous investigations, our knowledge of the properties of C/C composites and of their constituents, the well-known carbon fibers and pyrolytic carbon (pyC) matrices, remains limited to significantly lower temperatures. [5, 6, 7, 8, 9]. Therefore, the properties of interest – coefficients of thermal expansion, Young's moduli and Poisson coefficients along and normal to the fiber axes, etc. – have to be extrapolated to the temperatures of interest, which can be somehow heuristic.

Due to these extreme conditions that can be challenging, experiments are sometimes not suitable to identify and understand complex behaviors involved at the atomic and mesoscopic scales. To overcome this, virtual material approaches are becoming more and more popular. These approaches have indeed proven their value in understanding the thermo-mechanical and chemical behavior of high explosives [10, 11, 12], in investigating metals response under very high strain rates [13, 14, 15], as well as in studying the damage and mechanical behavior of ceramics and carbon composites [16, 17].

When bridging the gap between time and length scales, which is the essence of multiscale modeling, complex material architectures - as those in C/C composites - can be simulated under various thermodynamic conditions, provided one has a precise enough constitutive law for the individual elements of the microstructure. However, determining such constitutive laws under UHT conditions can be even more challenging than investigating the whole composite material, from the experimental point of view.

Atomistic simulation techniques, like molecular dynamics (MD) simulations, are, in theory, well-suited for such investigations. In the case of C/C composites, large-scale (2×10^5 atoms) atomistic models of the pyC matrices [18] have been proposed in recent years. However, their corresponding room temperature elastic constants [19] failed to reproduce the existing experimental data [8]. In particular, the longitudinal tensile moduli were significantly larger, by factors of 2 to 6, than the measurements, indicating that the models are either not accurate nor sufficiently large to properly capture the elastic behavior of the pyC. We note that, while currently no such atomistic model exist to describe the bulk properties of C fibers, some models of carbon fibers surfaces have been recently proposed [20].

Taking some distance with the accurate representation of actual C/C composites, we consider in this work the case of crystalline hexagonal graphite, which, conversely to the case of pyC matrices and carbon fibers, has a perfectly determined structure. Also, experimental

data only exists for the full elastic tensor of single crystalline graphite at room temperature [21, 22], which is not the case for fibers and matrices for which only longitudinal and transverse Young's moduli are generally reported. On the other hand, to the best of our knowledge, no experimental data is available concerning the elastic constants of graphite at elevated temperatures.

In this work we use MD simulations to determine the temperature dependence of graphite's unit cell lengths and elastic constants, which are fundamental parameters in deriving constitutive laws for up-scaled thermo-mechanical models of graphite-based complex architectures, inaccessible to atomic-scale modeling. Considering applications under somehow extreme conditions such as shock loading, high strain-rate deformation or thermal aggression, these properties are computed up to ultra high temperature, i.e. T = 4000 K, at ambient pressure, i.e. P = 1 atm. Also, two types of elastic constants, corresponding to drastically different conditions, are determined. On one hand, we compute the usual isothermal (or quasi-static) elastic constants, in which strain rate is low with respect to all elastic relaxation modes of the material. On the other hand, the so-called adiabatic elastic constants are computed, under the application of instantaneous deformations without any subsequent atomic positions relaxation. This method has already been used to compute the adiabatic elastic constants of the triclinic compound TATB [23]. As explained by Wallace [24] and Sutton [25], any given thermoelastic process should be associated with either adiabatic or isothermal elastic constants. However, whether it should be one or the other is directly related to the rate of elastic deformation. For example, adiabatic elastic constants are measured by ultrasonic pulse experiments while their isothermal counterpart are usually measured in direct quasi-static mechanical tests at constant temperature. The difference between adiabatic and isothermal elastic constants is in general temperature dependent, which will be shown in the present work. In the end, analytical formulations of both elastic tensors will be provided as a function of temperature, ready to be assigned to a continuum framework. However, if the later involves a physical process that requires both adiabatic and isothermal elastic moduli over various thermodynamic conditions, it should always be associated with corresponding thermal stress/strain tensors as well as specific heat.

While extended benchmarks of carbon potentials have been published in recent years [26, 27], the latter focused on the structure of quenched, then annealed, disordered carbons. So far, the abilities of such potentials to describe the lattice parameters and elastic constants of graphite, and their evolution upon increasing temperature remains mostly unknown. Therefore, and as no experimental data exists to validate the simulations, we consider five popular empirical potentials: REBO [28], AIREBO [29], AIREBO-M [30], CEDIP [31] and LCBOPII [32]. Comparison of the results obtained with these different potentials allows us to determine reliable trends on the high temperature elastic behavior of graphite.

2. Methods

2.1. Interatomic potentials

Empirical potentials are frequently used to investigate elastic and fracture properties of carbon-based systems [33, 34, 35]. Here we consider five potentials amongst the most widely used: REBO [28], AIREBO [29], AIREBO-M [30], CEDIP [31] and LCBOPII [32]. The reactive empirical bond order (REBO) potential of Brenner *et al.* [28] has been extensively used in the literature, mostly to investigate elasticity and fracture of nanocarbons, including graphene and carbon nanotubes [34, 36, 37]. The two versions of the adaptive intermolecular reactive bond order potential (AIREBO and AIREBO-M) from Stuart *et al.* [29] are directly derived from REBO. They complement the latter with a bond-order dependent integration of van der Waals interactions and a torsional potential around single C-C bonds to better describe hydrocarbons in the liquid state and aromatic stacking distances. In the AIREBO-M potential, the Lennard-Jones term used to describe van der Waals interactions in AIREBO - known to significantly overestimate repulsive forces under large compressive strains - is replaced with a more realistic Morse potential [30]. Another potential, namely SED-REBO [38] is available in the literature and based on the second generation of REBO. Since this potential is equivalent to REBO in terms of elasticity, it was not used in the present work. The last two potentials considered in the present work are the environment dependent interatomic potential for carbon (CEDIP) from Marks *et al.* [31] and the improved long-range carbon bond-order potential (LCBOPII) from Los *et al.* [32]. Conversely to the previously mentioned potentials in which bonding interactions are cut off at very short distances, via a switching function operating in the 1.7-2 Å range, medium-range interactions are included in the both CEDIP and LCBOPII potentials, which is a clear advantage for capturing fracture properties. Another major consequence of medium-range interactions is that these potentials allow for a quantitative prediction of the energy barrier for the graphite to diamond transition while potentials of the REBO family do not [39]. However, LCBOPII differs from CEDIP since it contains explicit long-range (dispersion) interactions while the former does not. Although these two potentials have been considerably less used than REBO or AIREBO potentials, a few reports suggest that these potentials are valuable candidates. Elastic and fracture properties of low temperature and annealed amorphous carbon have been investigated using CEDIP [40], while LCBOPII was used to study the pressure-induced graphite to diamond phase transformation under shock conditions and homothetic strain [41, 42, 43].

2.2. Molecular dynamics simulations

Two different classical molecular dynamics (MD) codes are used in this work. The LAMMPS (Large-scale Atomic/Molecular Massively Parallel Simulator) [44, 45] is used for all simulations using REBO, AIREBO, AIREBO-M and CEDIP potentials while the STAMP [46]

(Simulations Temporelles Atomistiques Massivement Parallélisées) code is used to perform simulations using LCBOPII potential as it is not currently implemented in LAMMPS. For both codes, MD trajectories are integrated using a velocity-Verlet integrator [47] and a 0.5 fs timestep, ensuring a correct energy conservation under equilibrium microcanonical (NVE) runs. Besides energy conservation tests, simulations are run in both canonical (NVT) and isothermal-isobaric (NPT) ensembles, using a Nosé-Hoover style thermostat [48, 49] and barostat [50] along with 0.1 ps and 1.0 ps damping constants, respectively. For the determination of graphite single crystal lattice parameters and elastic constants evolution with temperature, a 3D-periodic orthorhombic simulation cell containing 3456 carbon atoms is considered, consisting in a $6 \times 6 \times 6$ replication of the 16 atoms graphite orthorhombic unit cell. In Section 3.6, a 107520 atoms 3D-periodic simulation cell consisting in a $20 \times 24 \times 14$ replication of the same unit cell is considered to investigate the dynamical aspects of stress relaxation with sufficient statistics. In all the simulations, except the ones for computing the elastic constants that require a change in the simulation box shape, i.e. when applying shear strain, the cell angles are constrained to maintain a constant value of 90 %, accordingly to the graphite orthorhombic unit cell. For the simulations in the isothermal-isobaric ensemble, diagonal components of the stress tensor are controlled independently so that true hydrostatic conditions can be achieved, accordingly to the very large elastic anisotropy of graphite single crystal.

2.3. Lattice equilibration at finite temperature

For each potential, the system is equilibrated in the isothermal-isobaric (NPT) ensemble during 1 ns at a pressure of 1 atm and at 300 K and for temperatures ranging from 500 to 4000 K (i.e. close to graphite's melting point), by steps of 500 K. Lattice parameters are systematically averaged over the last 250 ps of the NPT trajectory, during which the stress tensor is checked to be fully hydrostatic, without any substantial evolution of simulation cell lengths. As both REBO and CEDIP potentials do not include van der Waals interactions, only the in-plane lattice parameters are allowed to evolve in the NPT simulations for these two potentials, the out-of-plane parameter were arbitrarily held fixed to the value obtained using the LCBOPII model at the considered temperature.

2.4. Elastic constants calculation

Graphite single crystal elasticity is known to possess a transverse isotropy symmetry, which is an elastic symmetry derived from the orthotropic elastic symmetry, for which the

second-order elastic tensor possesses 9 independent elastic components:

$$\boldsymbol{C} = \begin{pmatrix} C_{11} & C_{12} & C_{13} & 0 & 0 & 0 \\ C_{12} & C_{22} & C_{23} & 0 & 0 & 0 \\ C_{13} & C_{23} & C_{33} & 0 & 0 & 0 \\ 0 & 0 & 0 & C_{44} & 0 & 0 \\ 0 & 0 & 0 & 0 & C_{55} & 0 \\ 0 & 0 & 0 & 0 & 0 & C_{66} \end{pmatrix} \tag{1}$$

where the Voigt contraction convention has been used to represent the elastic tensor $\boldsymbol{C}$ as a second-order tensor. As an additional criterion to compare the results obtained with the different potentials, we first make the assumption that the graphite single crystal has an orthotropic symmetry, with 9 independent elastic constants. This hypothesis is always true because a material that possesses a transverse isotropic elasticity has by definition an orthotropic elasticity. However, for a material to have a transverse isotropic elasticity, it is required that, $C_{11} = C_{22}$, $C_{13} = C_{23}$, $C_{44} = C_{55}$ and $C_{66} = (C_{11} - C_{12})/2$, with all other components equal to zero. For graphite single crystal this implies that the elastic response to a deformation along the armchair or zigzag direction is strictly equivalent, which might not be true for certain potentials [36]. When a material is transversely isotropic, its second-order elastic tensor reads:

$$\boldsymbol{C} = \begin{pmatrix} C_{11} & C_{12} & C_{13} & 0 & 0 & 0 \\ C_{12} & C_{11} & C_{13} & 0 & 0 & 0 \\ C_{13} & C_{13} & C_{33} & 0 & 0 & 0 \\ 0 & 0 & 0 & C_{44} & 0 & 0 \\ 0 & 0 & 0 & 0 & C_{44} & 0 \\ 0 & 0 & 0 & 0 & 0 & (C_{11} - C_{12})/2 \end{pmatrix} \tag{2}$$

with 5 independent elastic component. In the following, we consider the general case with elastic orthotropic symmetry, in order to compare the elastic constants computed with different potentials, and determine whether they verify the transverse isotropic symmetry. By construction, it is necessary to apply 6 deformation types to get the full second-order elastic tensor from MD simulations. As for the lattice constant calculations, elastic constants involving the out-of-plane direction are not investigated with REBO and CEDIP. Mechanical properties are computed by applying an homothetic strain to the entire system with atomic positions being remapped into the box, followed or not by an equilibration in the NVT ensemble whether we aim at calculating isothermal or adiabatic elastic constants. The differences between the two methods are shortly explained in the following sections.

2.4.1. Isothermal elastic constants

Isothermal elastic constants are computed as follows. Starting from the equilibrium lattice parameters, a series of uniaxial engineering strains are uniformly applied to the graphite supercell. The considered strain range correspond to $\varepsilon \in [-0.3, +1.0]$ %, with a 0.1 % increment, for deformations along the principal axes, where negative and positive values correspond to compressive and tensile strains, respectively. Note that the lower range of compressive strain was chosen to avoid well-known compression-induced buckling elastic instabilities in anisotropic materials [51, 12, 43, 52]. Shear strains are applied in the $[-1.0, +1.0]$ % range with the same increment. After the strain is applied, the simulation cells are equilibrated in the NVT ensemble for 1.0 ns, leading to the stress relaxation of the the system through the relaxation of atoms positions. Stress tensors are then obtained by averaging stress components over the last 100 ps of the trajectories and isothermal elastic constants C_{ij}^{T} are determined via linear fits of the corresponding stress vs. strain curves.

2.4.2. Adiabatic elastic constants

Adiabatic elastic constants are obtained in a somehow opposite way. First, the system is equilibrated for 1 ns in the NVT ensemble using the equilibrium lattice parameters obtained from the NPT trajectory at 1 atm. Then, 20 independent configurations are selected from the last 100 ps of the NVT simulation, on which finite adiabatic strains, spanning the same values as those used in the isothermal case, are applied via pure homothethic transformations to the simulation cells. The resulting 20 uncorrelated stress-strain curves, for each deformation type, are then gathered to build the average stress-strain curve, from which the corresponding adiabatic, or isentropic elastic components C_{ij}^{S} are obtained, where the superscript ^{S} relates the elastic constant to entropy. This way, one deformation type gives directly access to 6 elastic constants.

3. Results

3.1. Room temperature lattice parameters

The lattice parameters of graphite single crystal at ambient temperature, i.e. P = 1 atm and T = 300 K, predicted using the different potentials are given in Table 1. Experimental data from Baskin and Meyer [53] are given for comparison. LCBOPII, REBO and CEDIP potentials lead to values of the in-plane lattice parameter (a) that are in excellent agreement with experiments, with a maximum deviation of 0.06 % obtained for CEDIP. On the other hand, AIREBO and AIREBO-M potentials show a significant underestimation of a, by ~ 1.6 %, which results from the reparametrization of the REBO term in AIREBO to compensate for the added torsional term which slightly destabilizes sp^2 carbon atoms [29]. Conversely, AIREBO and AIREBO-M give a better prediction of the inter-layer spacing ($d_{002} = 0.5c$)

while LCBOPII overestimates it by 1.6 %. As discussed above, no c values could be predicted using REBO and CEDIP.

Table 1: Lattice parameters of graphite at P = 1 atm and T = 3000 K computed using the different potentials and compared to the experimental reference [53]. Relative errors in % with respect to the reference are reported in parentheses.

	a (Å)	c (Å)
Exp.	2.4590	6.7076
LCBOPII	2.4590 (0.000)	6.8180 (1.646)
AIREBO	2.4193 (-1.615)	6.7078 (0.004)
AIREBO-M	2.4193 (-1.616)	6.7078 (0.003)
REBO	2.4600 (0.042)	N/A
CEDIP	2.4605 (0.059)	N/A

3.2. Room temperature elastic properties

Isothermal elastic constants computed at P = 1 atm and T = 300 K using the different potentials are compared in Table 2 to experimental values from two reference papers. It has been previously presented that some potentials may slightly deviate from the expected transverse isotropy symmetry of graphite when regarding elasticity [19, 36]. Hence, as discussed before, we adopt in the present work the general case of orthotropic symmetry of the second-order elastic tensor in order to compare the computed elastic constants of graphite single crystal.

Table 2: Isothermal elastic constants (in GPa) of graphite single crystal at P = 1 atm and T = 300 K computed using the different interatomic potentials under the assumption of an orthotropic elastic symmetry. The last column corresponds to the metric d_{ti}^{in} that is meant to measure the deviation from the transverse isotropy, computed from the in-plane components of the second-order elastic tensor.

	C_{11}	C_{22}	C_{33}	C_{12}	C_{13}	C_{23}	C_{44}	C_{55}	C_{66}	d_{ti}^{in}
Exp. [21]	1060.0		36.5	180.0	15.0		0.18		440.0	0.0
Exp. [22]	1109.0		38.7	139.0	0.0		5.0		485.0	0.0
LCBOPII	941.0	945.0	28.5	159.9	6.5	6.1	0.23	0.17	389.2	0.05
AIREBO	1000.9	1000.4	45.6	209.9	7.6	6.5	0.15	0.05	407.8	-1.54
AIREBO-M	936.5	913.1	29.6	190.4	7.6	7.9	0.04	0.01	406.2	-3.60
REBO	808.7	827.7	N/A	183.2	N/A	N/A	N/A	N/A	340.0	-5.19
CEDIP	920.6	921.40	N/A	252.9	N/A	N/A	N/A	N/A	334.6	-0.15

In a general way, all the force fields respect relatively well the hierarchy of the different elastic constants with $C_{11} > C_{66} > C_{12} > C_{33} > C_{13} > C_{44}$. The potentials also perform reasonably well from the quantitative perspective. Albeit being slightly lower than the experimental references, the error on computed C_{11} ranges from about 10 % with AIREBO to

about 27 % with REBO. As for C_{11}, C_{66} is underestimated by 8 to 15 % with AIREBO and AIREBO-M, the largest error, 24-30 %, being obtained for REBO and CEDIP. Regarding C_{12} the value predicted with LCBOPII, 159.9 GPa, is almost in the middle of the two experimental reference values, the other potentials predicting slightly larger values, the largest, 253 GPa, obtained with CEDIP being 40-80 % too large. Predicted C_{33} values are either about 7-8 GPa larger (AIREBO) or lower (LCBOPII, AIREBO-M) than the experimental data.

Concerning the shear elastic constants C_{44} and C_{55}, there is a large experimental spreading of the data since Bosak *et al.* [22] and Blakslee *et al.* [21] predicted values of 5 GPa and 0.18 GPa, respectively. LCBOPII, AIREBO and AIREBO-M potentials lead to consistent values in the 0-0.2 GPa range, i.e. close to the experimental data of Blakslee *et al.* [21]. However, more recent theoretical [54] and experimental investigations [55] suggest that the value of 5 GPa is correct for C_{44}, the lower values obtained on compressed pyrolytic graphite by Blakslee et al. being attributed to glissile basal dislocations. Therefore, it seems that all the considered potentials underestimate C_{44}. As for C_{13}, the three potentials predict values in the 6-8 GPa range, that are intermediates to the values of Blakslee *et al.* [21] and Bosak *et al.* [22], 15 and 0 GPa, respectively, and almost perfectly equal to the value of 7.9$\pm$3.5 recommended by Cousins and Heggie [54].

Two metrics are defined to identify the deviation from transverse isotropy symmetry, regarding in-plane and our-of-plane symmetry, respectively:

$$d_{ti}^{in} = 100 \times \left[1 - \frac{1}{2} \times \left(\frac{C_{11}^2 + C_{22}^2}{2C_{11}C_{22}} + \frac{2C_{66}}{2\frac{C_{11}^2+C_{22}^2}{C_{11}+C_{22}} - C_{12}} \right) \right] \tag{3}$$

$$d_{ti}^{out} = 100 \times \left[1 - \frac{1}{2} \times \left(\frac{C_{13}^2 + C_{23}^2}{2C_{13}C_{23}} + \frac{C_{44}^2 + C_{55}^2}{2C_{44}C_{55}} \right) \right] \tag{4}$$

where each ratio should be equal to 1 in the presence of an elastic tensor with transverse isotropy symmetry.

The values of d_{ti}^{in} are reported in the last column of Table 2, noticing that $d_{ti}^{in} = 0$ is expected experimentally. d_{ti}^{out} is not reported for the isothermal constants due to the very low values of C_{44}, and the necessarily large associated relative uncertainty. Amongst the different potentials LCBOPII is the one that produces the second-order elastic tensor with the closest symmetry to in-plane transverse isotropy, followed by CEDIP, the three other potentials showing much larger deviations.

In Table 3 are listed the adiabatic elastic constants computed with the different potentials. Since no experimental data correspond to adiabatic elastic constants measurements for graphite single crystal, we only discuss them in terms of their differences with isothermal elastic constants as well as their deviation from the transverse isotropy symmetry. As a

Table 3: Adiabatic elastic constants (in GPa) of graphite single crystal at P = 1 atm and T = 300 K computed using the different interatomic potentials under the assumption of an orthotropic elastic symmetry. The last two columns correspond the in-plane d_{ti}^{in} and out-of-plane d_{ti}^{out} metrics measuring the deviation from transverse isotropy.

	C_{11}	C_{22}	C_{33}	C_{12}	C_{13}	C_{23}	C_{44}	C_{55}	C_{66}	d_{ti}^{in}	d_{ti}^{out}
LCBOPII	1060.0	1061.0	32.3	116.6	3.8	4.2	5.9	5.8	471.7	-0.03	-0.26
AIREBO	1188.6	1188.5	48.5	98.9	4.2	4.2	7.0	7.0	544.6	0.02	0.0
AIREBO-M	1187.4	1186.8	32.2	99.1	3.0	3.1	7.5	7.4	543.8	0.05	-0.03
REBO	1058.9	1213.7	N/A	104.0	N/A	N/A	N/A	N/A	469.3	-3.62	N/A
CEDIP	1009.0	1009.3	N/A	181.5	N/A	N/A	N/A	N/A	413.0	0.08	N/A

general observation, and for all the potentials, the computed adiabatic elastic constants are much closer to the transverse isotropy symmetry than their isothermal counterparts, with one noticeable exception being the large C_{11}/C_{22} ratio, 1.146, obtained with REBO. One notice that the adiabatic values of C_{11} obtained with LCBOPII and REBO are almost perfectly identical to the the experimental data of Blakslee et al. [21], which indicates that these potentials have been calibrated to reproduced the elastic constants of graphite using homogeneous deformation without relaxation of atomic positions, i.e. under adiabatic conditions. In addition, all the potentials lead to a value of the adiabatic constant C_{66} that is higher than the isothermal constant, whereas the adiabatic constant C_{12} is lower than the isothermal value. Under the assumption that graphite single crystal is transversely isotropic, the relationship $C_{66} = (C_{11} - C_{12})/2$ holds and a decrease in C_{12} systematically involves an increase in C_{66}, which could explain the observed trend.

3.3. Temperature evolution of lattice parameters

Figure 1 compares the evolution with temperature of the lattice parameters computed using the different potentials to available experimental data [56, 57, 58, 59]. Common to all the potentials is the observation of a monotonous increase in the in-plane lattice parameter (a) with temperature (see Figure 1a), which conflicts with experimental results showing that a passes through a minimum at about 700 K. The slight contraction observed experimentally at low temperatures can indeed not be captured by classical MD as pointed out in recent investigations comparing classical and quantum, path integral, MD in the case of monolayer graphene [60, 61]. Besides this, all potentials seems to significantly overestimate both in-plane and out-of-plane thermal expansion, even at large temperatures, CEDIP being the closest to experimental data. Quantitatively, predicted a values using REBO, CEDIP and LCBOPII are very close to the commonly accepted experimental data of Kellet and Richards [62] at low temperatures and differ by less than ~ 1 % at T = 3000 K. Conversely, the values obtained for AIREBO and AIREBO-M are significantly lower, as already discussed above for the room temperature data.

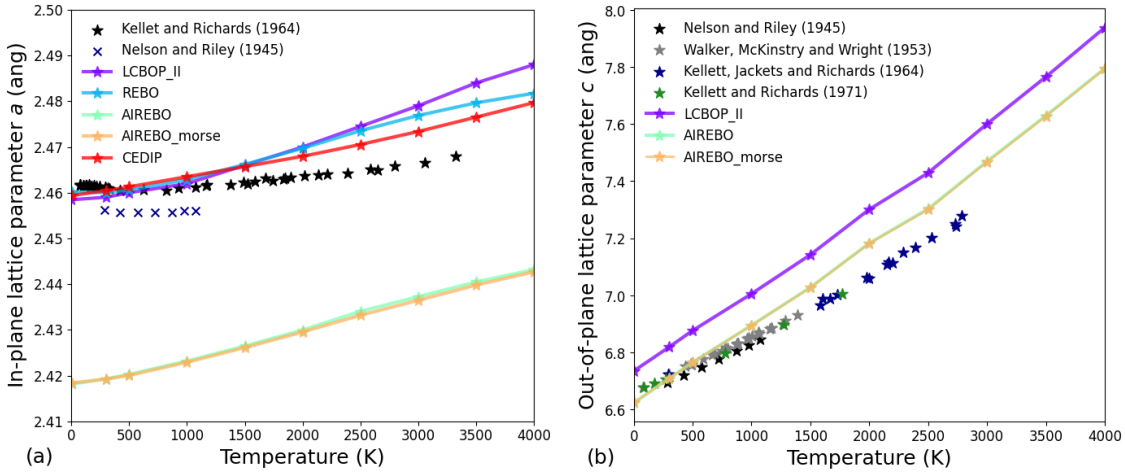

Figure 1: Evolution of (a) in-plane and (b) out-of plane lattice parameters with temperature obtained computed with the different potentials. Experimental data from Nelson and Riley [56], Kellet and Richards [62, 59], Walker, McKinstry and Wright [58] and Kellett, Jackets and Richards [57] are given for comparison.

The potentials considered for the out-of-plane lattice parameter (c), namely LCBOPII, AIREBO and AIREBO-M, reproduces well the monotonous expansion observed experimentally with increasing temperature (see Figure 1b). Quantitatively speaking, while all potentials slightly overestimate thermal expansion, AIREBO and AIREBO-M provide values that are closer to experimental data than LCBOPII. The relative errors to the experiment value from Kellett *et al.* [57] at T = 2500 K are of 0.5 % for AIREBO and AIREBO-M and of 1.95 % for LCBOPII.

3.4. Temperature evolution of elastic constants

Figure 2 shows the computed evolution with temperature of the six elastic coefficients defined above, assuming transverse isotropy elastic symmetry. Therefore C_{11}, C_{13} and C_{44} are taken as the mean values of equivalent orthotropic constants, $\frac{C_{11}+C_{22}}{2}$, $\frac{C_{13}+C_{23}}{2}$ and $\frac{C_{44}+C_{55}}{2}$, respectively. Regarding in the first place the in-plane stiffness, we observe that all related constants (C_{11}, C_{12} and C_{66}) decrease with increasing temperature. In the specific case of C_{11}, all potentials show an almost linear evolution (especially CEDIP), with a decrease of about 35-40 % when T decreases from 300 tp 4000 K, in agreement with the decrease of graphene's Young modulus recently predicted for graphene [63] using the SED-REBO potential [38]. The decrease in C_{11} obtained with CEDIP is slightly less pronounced, only reaching $\sim$ 25 % at T = 4000 K. The difference in behavior between CEDIP and the four other potentials is significant when regarding C_{12} and C_{66}. As for C_{11}, a linear decrease in C_{12} is observed for CEDIP, from about 250 to 220 GPa and from 335 to 230 GPa for C_{66} when T increases from 300 to 4000 K. The other potentials show much lower values for C_{12} and a clearly non-linear evolution with a strong decrease at low temperatures, from values scattered

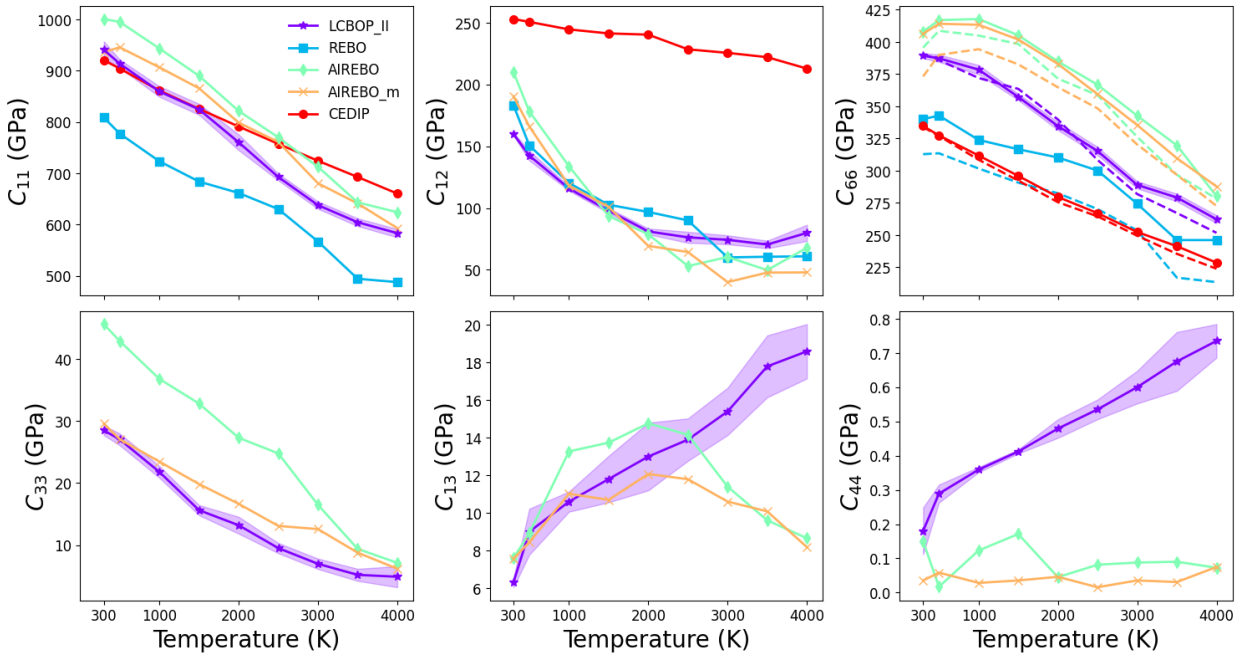

Figure 2: Evolution with temperature of the isothermal elastic constants of graphite single crystal at P = 1 atm computed using the different potentials. For clarity, error bars are only given for data obtained with the LCBOPII potential. Error bars for the other data sets are expected to be of the same order. Dashed lines for C_{66} data correspond to predictions obtained from C_{11} and C_{12} assuming transverse isotropy symmetry.

in the 160-210 GPa range at 300 K, down to a plateau at large temperatures with values contained in the 50-80 GPa range. Conversely, the other potentials give values for C_{66} that are larger than those obtained with CEDIP. Furthermore, AIREBO and AIREBO-M show a non-monotonous behavior at low temperatures, with values that first increase, then decrease with increasing T. Values obtained at 4000 K for C_{66} range from 230 GPa (CEDIP) to $\sim$ 280 GPa (AIREBO, AIREBO-M). In Figure 2, we also represent the analytical C_{66} component, computed from the relation $C_{66} = (C_{11} - C_{12})/2$ for transverse isotropy symmetry, using dashed lines for every potential used. This shows directly that, under isothermal conditions, CEDIP and LCBOPII provide a good estimation of C_{66} for the transverse isotropy symmetry, whereas for REBO and AIREBO potentials, the computed value shifts from the analytical expression.

Now focusing on the elastic constants involving interlayer interactions, we observe that C_{33} is the most sensitive to an increase in temperature, with values dropping, more or less linearly, by a factor of $\sim$ 5-6 when increasing T from 300 to 4000 K, whatever the potential. Unlike C_{33}, the behavior with increasing T of C_{13} and C_{44} significantly depends on the potential. While with LCBOPII, C_{13} almost linearly increases from 6 GPa at 300 K to $\sim$ 18 GPa at 4000 K with LCBOPII, it evolves from 7.5 GPa at 300 K to 9 GPa at 4000 K with AIREBO

and AIREBO-M by passing through maximum values of about 15 and 12 GPa at T = 2000 K, with AIREBO and AIREBO-M, respectively. Finally, while C_{44} continuously increases from 0.2 GPa at 300 K to 0.7 GPa at 4000 with LCBOPII, it remains more or less constant, at around 0.1 and 0.05 GPa with AIREBO and AIREBO-M, respectively.

The temperature evolution of adiabatic elastic constants is shown in Figure 3. As explained before, the adiabatic elastic constants are calculated by applying instantaneous deformations to an MD simulation cell that has been equilibrated in the NVT ensemble at zero deformation and target temperature. It then catches the instantaneous elastic response of a material and is cost-less compared to the calculation procedure of isothermal elastic constants that requires en equilibration in the NVT ensemble for each value of the deformation.

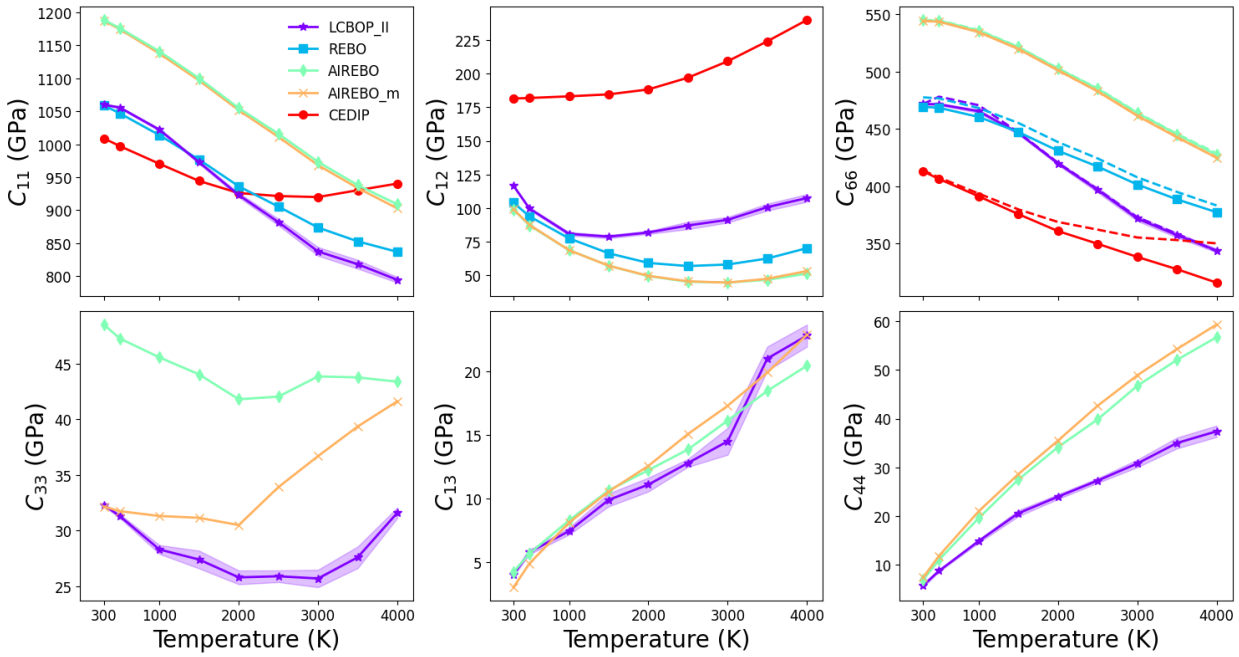

Figure 3: Same as Figure 2 for the adiabatic elastic constants.

All the potiential but CEDIP show a continuous decrease of C_{11} with increasing T, up to about 20 to 25 % at 4000 K, in an almost linear fashion, at least for AIEBO and AIREBO-M. Conversely, the decrease in C_{11} obtained with CEDIP is only of about 5 %, and non monotonous, with a minimum value observed around 2500-3000 K. C_{12} also shows similar evolutions with REBO, AIREBO, AIREBO-M and LCBOPII, first decreasing down to minimum values at about 1000-1500 K with LCBOPII and 2000-2500 K with REBO, AIREBO and AIREBO-M, before increasing again. At 4000 K, C_{12} has decreased of about 50 % with AIREBO and AIREBO-M, 30 % with REBO, and 10 % with LCBOPII with respect to the 300 K values. Again, CEDIP is an outlier with respect to the other potentials, with C_{12} continuously increasing, although non monotonically, with T, showing an increase of about

33 % over the considered T range. Regarding C_{66} all potentials show a similar monotonous decreasing trend, with values at 4000 K that are $\sim$ 20-25 % lower that at 300 K, LCBOPII showing the larger and less-linear decrease. Also, all the potentials satisfy well the transverse isotropy constraint, apart from CEDIP at large temperatures.

The three potentials considered for C_{13} show a similar, close to linear, increase with increasing T, from about 3-4 GPa at room temperature, to about 20-24 GPa at 4000 K. Similarly, C_{44} significantly increase with T, yet in a sublinear fashion, from about 6-7 GPa at room temperature, to $\sim$ 60 GPa with AIREBO and AIREBO-M, and 35 GPa with LCBOPII, at 4000 K. The behavior observed for C_{33} is less clear, with a non-montonous evolution observed for all potentials, showing considerably less variation in values than for C_{13} and C_{44}.

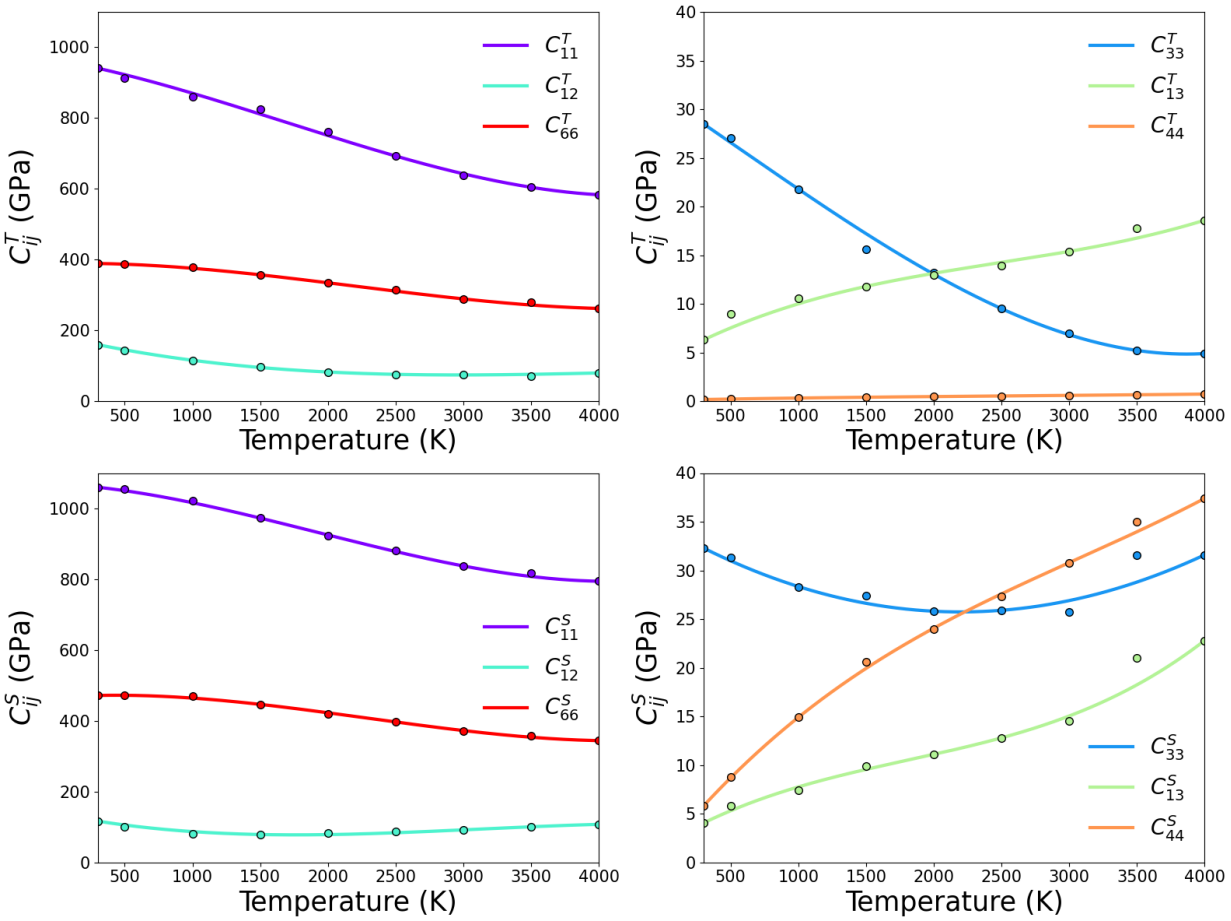

Figure 4: Comparison of MD data and polynomial fits for the temperature dependence of the isothermal and adiabatic elastic constants. symbols: MD data; lines: polynomial fits.

Due to the non-linear evolution of graphite single crystal elasticity (both isothermal and adiabatic) with temperature, we propose an analytical expression for this dependency based on polynomial fits. For the sake of simplicity, only the LCBOPII potential is considered in

the remaining of the manuscript. Indeed, this potential was shown to produce reasonable lattice parameters and elastic constants, preserving well the trnsverse isotropy of graphite. Furthermore, it allows to capture out-of-plane elastic constants, which CEDIP and REBO cannot. We take the condition T_{ref} = 300 K as the reference configuration, leading to the following formulation of the isothermal/adiabatic spatial elasticity tensor along the ambient pressure isobaric pathway:

$$\boldsymbol{c}^{S/T}(T) = \boldsymbol{c}^{S/T}_{ref}(T_{ref})\Big(\boldsymbol{I} + \sum_{k=1}^{N} \boldsymbol{A}_k (T - T_{ref})^k\Big) \tag{5}$$

where $\boldsymbol{c}^{S/T}_{ref}$ is the stiffness tensor at the reference state, with superscripts S and T corresponding to isothermal and adiabatic forms, respectively. $\boldsymbol{A}^k$ is a tensor containing the polynomial fit coefficients and N is taken equal to 3. It is to be noted that the product between $\boldsymbol{c}^{S/T}_{ref}$ and $\boldsymbol{A}^k$ is done through the Hadamard product, i.e. component-wise.

The temperature-dependent isothermal and adiabatic elastic coefficients and their corresponding polynomial fits are represented in Figure 4. In addition, the polynomial coefficients for both isothermal and adiabatic elastic tensors are provided in the supplementary material.

3.5. Temperature dependence of elastic anisotropy

When dealing with highly anisotropic materials like graphite, different metrics computed from the elastic tensor can help to discriminate whether the proposed analytical formulation is reliable or not. One of these metrics is the universal anisotropy index [64] which computes the level of anisotropy of any material from its elastic constants. It is based on the bulk and shear moduli computed using the Voigt and Reuss approximation. The Voigt bound relates to the behavior of a material under an isotropic deformation-imposed process while the Reuss bound is related to the behavior of a material under an imposed hydrostatic pressure. It is obvious that any isotropic material will behave in the same way under both conditions. Yet, this is not the case in the presence of anisotropy. The universal anisotropy index reads:

$$A^U = \boldsymbol{c} : \boldsymbol{s} = 5\frac{G^V}{G^R} + \frac{K^V}{K^R} - 6, \tag{6}$$

which takes a value of 0 for an isotropic material, since Voigt and Reuss estimates for bulk (K) and shear (G) modulus are identical. Figure 5 shows the evolution with temperature of A_{univ} along the 1 atm isobaric pathway computed from MD data and the isothermal and adiabatic analytical expressions.

First, we see that analytical formulations reproduce well both isothermal and adiabatic MD data, thus validating the polynomial fits. More importantly, Figure 5 shows that the elastic anisotropy is severely temperature dependent. At ambient temperature, anisotropy is very high compared to a large panel of materials [64, 65] and takes values of approximately

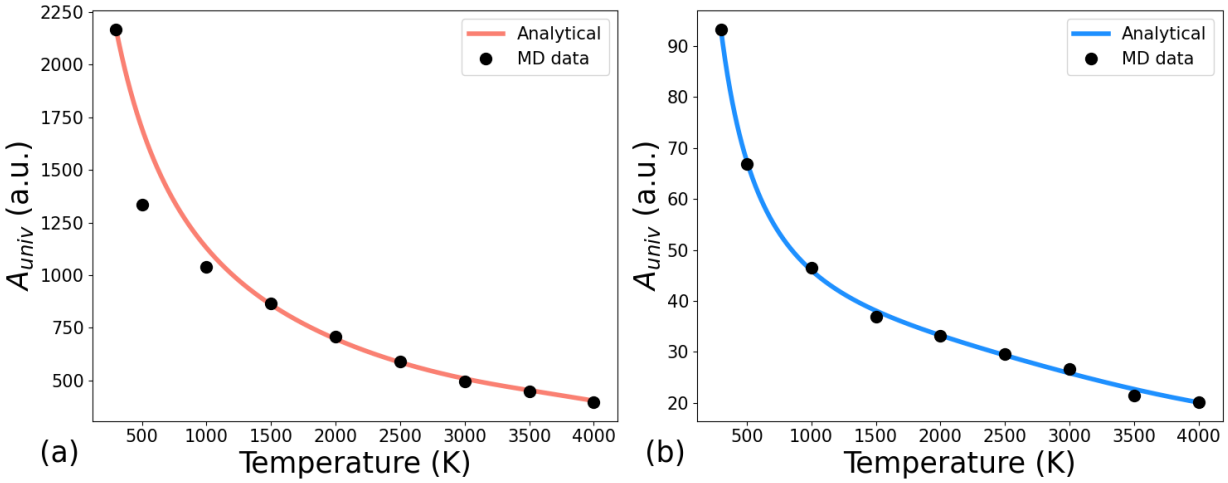

Figure 5: Universal Anisotropy Index as a function of temperature computed from (a) isothermal and (b) adiabatic elastic tensors, comparison between analytical formulation and MD data. All data were obtained with the LCBOPII potential.

93 and 2169 in adiabatic and isothermal conditions, respectively. Concerning the evolution with temperature, the isothermal anisotropy decreases non-linearly with temperature and is divided by almost a factor of 5.40 at 4000 K with respect to the 300 K case. The adiabatic anisotropy follows a very similar evolution and the ratio between the 300 K and the 4000 K values is around 4.65.

3.6. Adiabatic vs. isothermal elastic constants: relationship and implications

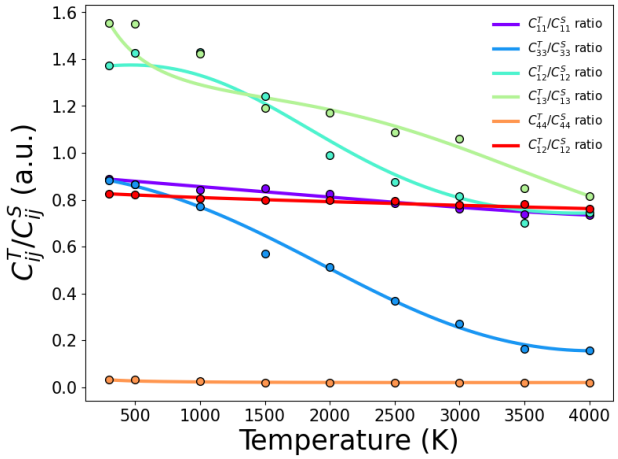

Figure 6: Evolution of the ratio between isothermal (C_{ij^T}) and adiabatic (C_{ij}^S) elastic constants of graphite single crystal using the LCBOPII potential as a function of temperature. All data were obtained with the LCBOPII potential.

We show in Figure 6 the ratios of the isothermal over adiabatic elastic constants as a function of temperature. Interestingly, these ratios remain almost constant for C_{11}, C_{66} and C_{44}, with values around 0.8 for C_{11} and C_{66}, and about 0.02 for C_{44}, although a slight linear decrease with increasing T is observed, especially for C_{11}. Here it is important to note that any value different from unity of the $\frac{C_{ij}^T}{C_{ij}^S}$ ratio indicates that stress relaxation will take place during, or after, deformation, depending on the deformation rate. For instance, the value of ~ 0.8 obtained for C_{11} indicates that when single crystalline graphite is subjected to a fast uniaxial in-plane deformation, the increase in stress is systematically followed by a relaxation process. In other words, this means that the measured elastic tensor will depend on strain rate, with the adiabatic and isothermal constants constituting the instantaneous and quasi-static limits, respectively. Similarly, the extremely low value of the isothermal over adiabatic ratio for C_{44} implies a systematic accommodation of interlayer shear deformation at large times.

Conversely to the formerly discussed constants, the isothermal over adiabatic ratio significantly decreases with T, with a close to linear dependency, for the three other constants, indicating that stress relaxation is strongly temperature-dependent for these constants. Ratios for C_{12} and C_{13} both decrease from about 1.5 at 300 K to about 0.8 at 4000 K, while for C_{33} a decrease from about 0.85 at 300 K to about 0.15 at 4000 K is observed.

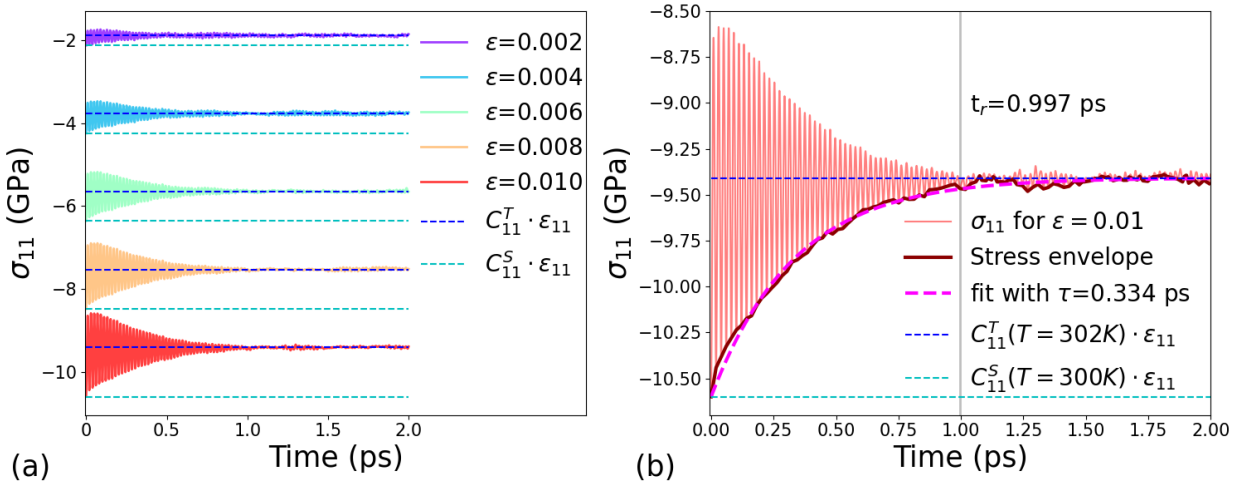

Figure 7: Evolution of **(a)** the stress component σ_{11} vs time after an instantaneous tensile strain ε_{11} is applied to the sample, for different values of ε_{11}. The blue and cyan dashed lines represent the limit values, corresponding to the analytic stress level using the isothermal and adiabatic C_{11} coefficients, respectively. **(b)** Focus on the case $\varepsilon_{11} = 0.01$. The dark red line is the computed limit envelope of the stress signal over time while the pink dashed line is the result of the fitted exponential decay function, with characteristic time τ. The vertical gray line corresponds to the relaxation time t_r computed as described in the text.

In order to understand the transition from adiabatic to isothermal elastic response, we used MD simulations with the LCBOPII potential to study the mechanical response of a graphite

single crystal at various temperatures and strain amplitudes. A graphite single crystal of approximate dimensions $10 \times 10 \times 10$ nm^3 containing 107520 atoms was equilibrated in the NVT ensemble for 50 ps for temperatures between 300 K and 4000 K. After the material is fully equilibrated, it is instantaneously dilated along the [100] direction for different strains ε between 0.1 % and 1 % in order to remain within the elastic domain, similar to the one used to compute the elastic constants. This deformation process is performed without any thermostat coupling in order to let the material relax over time without impacting the relaxation kinetics, which might be related to the thermostat damping constant. However, the deformation induced relaxation systematically involves heating of the system due to the total energy conservation. Yet, this process allows capturing the dynamics of the elastic response. Indeed, when the deformation is applied, the stress level is directly related to the adiabatic elastic constant C_{11}^S at the temperature right before the deformation, while after the relaxation process, the stress level corresponds to the isothermal elastic constant C_{11}^T at the temperature at the end of the relaxation process. What happens in between is then directly related to the transition between adiabatic and isothermal elastic response. Performing this procedure at different initial temperatures and different strains allows to identify how these conditions affect the transition, which can be related to the relaxation process behind the front of a shock-wave for example. In Figure 7, we display the time evolution of the stress component σ_{11}, for different longitudinal strains ε_{11} up to 1 %. The different blue and cyan dashed lines correspond to the analytical limits σ_{11}^{∞} and σ_{11}^{0} computed from isothermal and adiabatic elastic constants using linear elasticity:

$$\sigma_{11}^{0} = C_{11}^{S}(T_0) \cdot \varepsilon_{11}, \tag{7}$$

$$\sigma_{11}^{\infty} = C_{11}^{T}(T_{\infty}) \cdot \varepsilon_{11}. \tag{8}$$

where T_0 and T_{∞} correspond to the temperatures right before the deformation is applied and at the end of the relaxation process, respectively. A focus on the case $\varepsilon_{11} = 0.01$ is displayed in Figure 7, where the good agreement between the stress levels and the analytical values can be seen. However, one can see that the stress is oscillating around σ_{11}^{∞} while decreasing in amplitude over time. This oscillation of the stress is due to the elastic energy stored in the material at the instantaneous deformation that is relaxing through elastic waves emissions. In order to extract a characteristic time from this temporal evolution, the first step consists in extracting the envelope of the stress signal, that is directly related to the decrease of the stress over time. We then consider the following exponential decay function that relates the stress versus time to the isothermal and adiabatic elastic constants using the previously

defined analytical limits:

$$\sigma_{11}(t) = \sigma_{11}^{\infty} + (\sigma_{11}^{0} - \sigma_{11}^{\infty}) \exp(-t/\tau) \tag{9}$$

with τ the characteristic time associated to the exponential decay. We then define the characteristic relaxation time t_r as the time at which the decrease is completed at 95 %. The relaxation time for an initial temperature of 300 K and $\varepsilon = 0.01$ is displayed as a vertical gray line on Figure 7b. This procedure has been applied to stress signals for different strains $\varepsilon_{11} \in [0.001, 0.1]$ and for temperatures T $\in$ [300 K, 4000 K]. Figure 8a shows that the relaxation time t_r for instantaneous in-plane tensile loads is in the ps range for the considered strain and temperature range and that it increases with applied strain while it decreases with temperature. In addition, it is also interesting to discuss elastic relaxation in terms of its characteristic length:

$$L_r(T, \varepsilon) = t_r(T, \varepsilon) \sqrt{C_{11}^{T}(T)/\rho(T)} \tag{10}$$

where the square root term corresponds to the longitudinal elastic wave velocity of graphite, computed from the ratio between the isothermal elastic constant $C_{11}^{T}(T)$ and the density $\rho(T)$ at finite temperature.

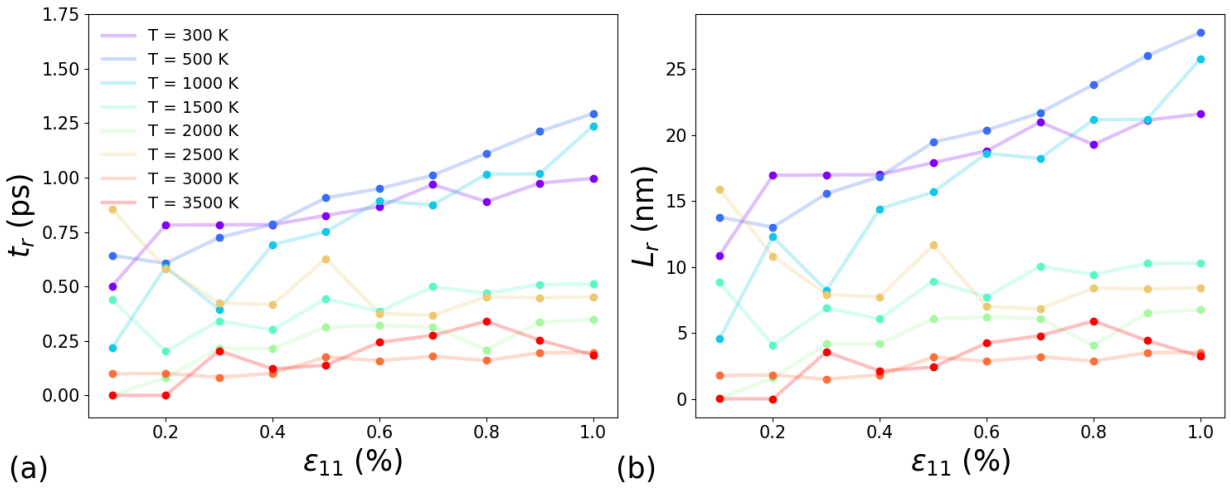

Figure 8: Evolution with strain and temperature of the characteristic **(a)** time and **(b)** length of the adiabatic to isothermal elastic stress relaxation after uniaxial in-plane compression. All data were obtained using the LCBOPII potential.

As shown in Figure 8b, similarly to t_r, L_r evolves slightly with temperature, reaching sort of a plateau at large strains. Indeed, the lower bound of this characteristic length remains below 10 nm at $\varepsilon_{11} = 0.01$ for temperatures above 1000 K while it is always below 25 nm for the entire set of simulations. This implies that, when a tensile (for example after a reflection) shock-wave propagates along [100] direction in a graphite single crystal, a slab of width < L_r

= 15 nm behind the front is required to accommodate the local high strain-rate and to transit from adiabatic to isothermal conditions. When considering high strain-rate deformation, one can talk in terms of relaxation time instead of characteristic length, since no discontinuities of particle velocities exist in the material. This would mean that if the dynamic deformation process involves local deformations above 1 % within a time window lower than a few ps, the process could be considered as adiabatic. On the other hand, a transition from adiabatic to isothermal would be involved.

4. Discussion and conclusion

Equilibrium MD simulations of graphite single crystal have been performed on an extended thermodynamic domain (up to 4000 K) at ambient pressure using various potentials of the literature, namely REBO, AIREBO, AIREBO-M, CEDIP and LCBOPII. The lattice parameters evolution with temperature has been computed with the different models and the LCBOPII model has been identified as a good candidate to represent the thermal behavior of graphite single crystal. Additionally, at each temperature, the spatial isothermal and adiabatic elasticity tensors have been computed through the derivation of the Cauchy stress with respect to strain, using the different models considered in this work. Adiabatic elastic constants correspond to the instantaneous response of a material to a mechanical deformation of very short wavelength, i.e. as found in the vicinity of the shock-wave front or during very high strain-rate deformation. On the opposite, isothermal elastic constants correspond to a fully equilibrated mechanical response at longer time scales, i.e. after a shock-wave has passed or under quasi-static or low strain-rate deformations.

Through the entire temperature range, both isothermal and adiabatic elastic coefficients are found to evolve non-linearly with temperature, independently from the potential used. Based on the good agreement with the literature for both lattice parameters evolution with temperature and for ambient temperature isothermal elastic constants, the LCBOPII model seems appropriate to study the mechanical behavior of graphite at high temperature. An analytical formulation for both isothermal and adiabatic spatial elasticity tensors as a function of temperature has been introduced as a preliminary element in order to build a mesoscopic model for the elastic behavior of graphite single crystal. The dependence on temperature is reproduced through a component-wise third-order polynomial fit using the Hadamard product, allowing to interpolate the elastic coefficients calculated using MD simulations.

Interestingly, it has been observed that isothermal and adiabatic elastic constants significantly differ from each other. A clear consequence of that is the difference in the elastic anisotropy of graphite, the universal anisotropy index being larger by a factor of ~ 20 in the isothermal case than in the adiabatic case, whatever the temperature. Also, temperature has a tremendous influence on elastic anisotropy with a decrease by a factor of five of the

universal anisotropy index observed between 300 K and 4000 K. This is of high importance since it has been shown that elastic softening deformation mechanisms such as elastic instabilities and in particular buckling are driven by the material anisotropy [51, 12, 43, 52]. The presented results actually suggest that such buckling transition may be suppressed at high temperatures and/or under adiabatic conditions.

Finally, MD simulations were used to investigate the details of the adiabatic to isothermal elastic relaxation by imposing an instantaneous deformation to a graphite single crystal at different temperatures and strain levels. The simulations suggest that in the presence of a tensile shock-wave going through a graphite crystal, a non negligible width of $\sim$ 20 nm is required to accommodate a 1 % instantaneous in-plane tension applied to graphite at room temperature and to allow the local material state to transit from adiabatic to isothermal stress response. Overall, this study provided a detailed, temperature dependent, analytic model of the adiabatic and isothermal elasticity of single crystalline graphite, that can be integrated into mesoscale models of graphite-based materials elasticity.

5. Acknowledgments

The authors would like to thank Dr. Christophe Denoual and Dr. Nicolas Pineau for their help in both setting up the MD simulations using the LCBOPII potential and discussing the results. This research is financially supported by the French Ministry of Defence - Defence Innovation Agency. Atomistic simulations were performed using the computational resources of the TGCC-CEA.

References

[1] J. Couzi, J. de Winne, B. Leroy, Improvements in Ablation Predictions for Reentry-Vehicles Nosetip, in: R. A. Harris (Ed.), Aerothermodynamics for space vehicles, Vol. 426 of ESA Special Publication, 1999, p. 493.

[2] I. L. Shabalin, Ultra-high temperature materials II, Springer, 2019.

[3] G. Savage, Carbon/Carbon composites, Chapman & Hall, London, 1993.

[4] C. Scarponi, Carbon–carbon composites in aerospace engineering, in: S. Rana, R. Fangueiro (Eds.), Advanced Composite Materials for Aerospace Engineering, Woodhead Publishing, 2016, pp. 385–412. doi:10.1016/B978-0-08-100037-3.00013-4.

[5] M. Trinquecoste, J. Carlier, A. Derré, P. Delhaès, P. Chadeyron, High temperature thermal and mechanical properties of high tensile carbon single filaments, Carbon 34 (7) (1996) 923–929. doi:10.1016/0008-6223(96)00052-8.

[6] C. Sauder, J. Lamon, R. Pailler, Thermomechanical properties of carbon fibres at high temperatures (up to 2000 °C), Compos. Sci. Technol. 62 (4) (2002) 499–504. doi:10.1016/S0266-3538(01)00140-3.

[7] C. Sauder, J. Lamon, R. Pailler, The tensile behavior of carbon fibers at high temperatures up to 2400 °C, Carbon 42 (4) (2004) 715–725. doi:10.1016/j.carbon.2003.11.020.

[8] C. Sauder, J. Lamon, R. Pailler, The tensile properties of carbon matrices at temperatures up to 2200°c, Carbon 43 (10) (2005) 2054–2065. doi:10.1016/j.carbon.2005.03.020.

[9] C. Pradere, C. Sauder, Transverse and longitudinal coefficient of thermal expansion of carbon fibers at high temperatures (300–2500k), Carbon 46 (14) (2008) 1874–1884. doi:10.1016/j.carbon.2008.07.035.
[10] M. P. Kroonblawd, L. E. Fried, High explosive ignition through chemically activated nanoscale shear bands, Phys. Rev. Lett. 124 (2020) 206002. doi:10.1103/PhysRevLett.124.206002.
[11] M. P. Kroonblawd, B. A. Steele, M. D. Nelms, L. E. Fried, R. A. Austin, Anisotropic strength behavior of single-crystal tatb, Model. Simul. Mat. Sci. Eng. 30 (1) (2021) 014004. doi:10.1088/1361-651X/ac3ca4.
[12] P. Lafourcade, C. Denoual, J.-B. Maillet, Mesoscopic constitutive law with nonlinear elasticity and phase transformation for the twinning-buckling of tatb under dynamic loading, Phys. Rev. Mater. 3 (2019) 053610. doi:10.1103/PhysRevMaterials.3.053610.
[13] L. A. Zepeda-Ruiz, A. Stukowski, T. Oppelstrup, V. V. Bulatov, Probing the limits of metal plasticity with molecular dynamics simulations, Nature 550 (7677) (2017) 492–495. doi:10.1038/nature23472.
[14] L. A. Zepeda-Ruiz, A. Stukowski, T. Oppelstrup, N. Bertin, N. R. Barton, R. Freitas, V. V. Bulatov, Atomistic insights into metal hardening, Nat. Mater. 20 (3) (2020) 315–320. doi:10.1038/s41563-020-00815-1.
[15] E. van der Giessen, P. A. Schultz, N. Bertin, V. V. Bulatov, W. Cai, G. Csányi, S. M. Foiles, M. G. D. Geers, C. González, M. Hütter, W. K. Kim, D. M. Kochmann, J. LLorca, A. E. Mattsson, J. Rottler, A. Shluger, R. B. Sills, I. Steinbach, A. Strachan, E. B. Tadmor, Roadmap on multiscale materials modeling, Model. Simul. Mat. Sci. Eng. 28 (4) (2020) 043001. doi:10.1088/1361-651X/ab7150.
[16] V. Mazars, O. Caty, G. Couégnat, A. Bouterf, S. Roux, S. Denneulin, J. Pailhès, G. L. Vignoles, Damage investigation and modeling of 3d woven ceramic matrix composites from x-ray tomography in-situ tensile tests, Acta Mater. 140 (2017) 130–139. doi:https://doi.org/10.1016/j.actamat.2017.08.034.
[17] A. P. Gillard, G. Couégnat, S. Chupin, G. L. Vignoles, Modeling of the non-linear mechanical and thermomechanical behavior of 3d carbon/carbon composites based on internal interfaces, Carbon 154 (2019) 178–191. doi:10.1016/j.carbon.2019.07.101.
[18] B. Farbos, P. Weisbecker, H. E. Fischer, J.-P. Da Costa, M. Lalanne, G. Chollon, C. Germain, G. L. Vignoles, J.-M. Leyssale, Nanoscale structure and texture of highly anisotropic pyrocarbons revisited with transmission electron microscopy, image processing, neutron diffraction and atomistic modelling, Carbon 80 (2014) 472–489.
[19] B. Farbos, J.-P. Da Costa, G. L. Vignoles, J.-M. Leyssale, Nanoscale elasticity of highly anisotropic pyrocarbons, Carbon 94 (2015) 285–294.
[20] F. Vuković, T. Walsh, Practical atomistic models of carbon fiber surfaces with tuneable topology and topography, Compos. Sci. Technol. 216 (2021) 109049. doi:https://doi.org/10.1016/j.compscitech.2021.109049.
[21] O. L. Blakslee, D. G. Proctor, E. J. Seldin, G. B. Spence, T. Weng, Elastic constants of compression-annealed pyrolytic graphite, J. Appl. Phys. 41 (1970) 3373–3382.
[22] A. Bosak, M. Krisch, Elasticity of single-crystalline graphite: Inelastic x-ray scattering study, Phys. Rev. B 75 (2007) 153408.
[23] P. Lafourcade, C. Denoual, J.-B. Maillet, Dislocation core structure at finite temperature inferred by molecular dynamics simulations for 1,3,5-triamino-2,4,6-trinitrobenzene single crystal, J. Phys. Chem. C 121 (13) (2017) 7442–7449. doi:10.1021/acs.jpcc.6b11576.
[24] D. Wallace, Thermodynamics of Crystals, Wiley, 1972.
[25] A. Sutton, Physics of Elasticity and Crystal Defects, Oxford Series on Materials Modelling, OUP Oxford, 2020.
[26] C. de Tomas, I. Suarez-Martinez, N. A. Marks, Graphitization of amorphous carbons: A comparative study of interatomic potentials, Carbon 109 (2016) 681–693.

570 doi:https://doi.org/10.1016/j.carbon.2016.08.024.
571 [27] C. de Tomas, A. Aghajamali, J. L. Jones, D. J. Lim, M. J. López, I. Suarez-Martinez,
572 N. A. Marks, Transferability in interatomic potentials for carbon, Carbon 155 (2019) 624–634.
573 doi:https://doi.org/10.1016/j.carbon.2019.07.074.
574 [28] D. W. Brenner, O. A. Shenderova, J. A. Harrison, S. J. Stuart, B. Ni, S. B. Sinnott, A second-generation
575 reactive empirical bond order (rebo) potential energy expression for hydrocarbons, J. Phys.: Condens.
576 Matt. 14 (4) (2002) 783–802.
577 [29] S. J. Stuart, A. B. Tutein, J. A. Harrison, A reactive potential for hydrocarbons with intermolecular
578 interactions, J. Chem. Phys. 112 (14) (2000) 6472–6486.
579 [30] T. C. O'Connor, J. Andzelm, M. O. Robbins, Airebo-m: A reactive model for hydrocarbons at extreme
580 pressures, J. Chem. Phys. 142 (2) (2015) 024903. doi:10.1063/1.4905549.
581 [31] N. A. Marks, Generalizing the environment-dependent interaction potential for carbon, Phys. Rev. B 63 (3)
582 (2001) 035401.
583 [32] J. H. Los, L. M. Ghiringhelli, E. J. Meijer, A. Fasolino, Improved long-range reactive bond-order potential
584 for carbon. i. construction, Phys. Rev. B 72 (2005) 214102.
585 [33] R. Grantab, V. B. Shenoy, R. S. Ruoff, Anomalous strength characteristics of tilt grain boundaries in
586 graphene, Science 330 (6006) (2010) 946–948.
587 [34] P. Zhang, L. Ma, F. Fan, Z. Zeng, C. Peng, P. E. Loya, Z. Liu, Y. Gong, J. Zhang, X. Zhang,
588 P. M. Ajayan, T. Zhu, J. Lou, Fracture toughness of graphene, Nat. Commun. 5 (2014) 3782.
589 doi:10.1038/ncomms4782.
590 [35] A. Gamboa, B. Farbos, P. Aurel, G. L. Vignoles, J.-M. Leyssale, Mechanism of strength reduction along
591 the graphenization pathway, Sci. Adv. 1 (10) (2015) e1501009.
592 [36] A. Gamboa, G. L. Vignoles, J.-M. Leyssale, On the prediction of graphene's elastic properties with reactive
593 empirical bond order potentials, Carbon 89 (2015) 176–87.
594 [37] Q. Lu, W. Gao, R. Huang, Atomistic simulation and continuum modeling of graphene nanoribbons
595 under uniaxial tension, Model. Simul. Mat. Sci. Eng. 19 (5) (2011) 054006. doi:10.1088/0965-
596 0393/19/5/054006.
597 [38] R. Perriot, X. Gu, Y. Lin, V. V. Zhakhovsky, I. I. Oleynik, Screened environment-dependent reactive
598 empirical bond-order potential for atomistic simulations of carbon materials, Phys. Rev. B 88 (2013)
599 064101.
600 [39] J. H. Los, N. Pineau, G. Chevrot, G. Vignoles, J.-M. Leyssale, Formation of multiwall fullerenes from
601 nanodiamonds studied by atomistic simulations, Phys. Rev. B 80 (2009) 155420.
602 [40] C. de Tomas, I. Suarez-Martinez, N. A. Marks, Carbide-derived carbons for dense and tunable 3d graphene
603 networks, Appl. Phys. Lett. 112 (25) (2018) 251907. doi:10.1063/1.5030136.
604 [41] N. Pineau, Molecular dynamics simulations of shock compressed graphite, J. Phys. Chem. C 117 (2013)
605 12778–12786.
606 [42] N. Pineau, L. Soulard, L. Colombet, T. Carrard, A. Pellé, P. Gillet, J. Clérouin, Molecular dynamics
607 simulations of shock compressed heterogeneous materials. ii. the graphite/diamond transition case for
608 astrophysics applications, J. Appl. Phys. 117 (2015) 115902.
609 [43] P. Lafourcade, C. Denoual, J.-B. Maillet, Elastic instability in graphite single crystal under dynamic triaxial
610 compression: Effect of strain-rate on the resulting microstructure, J. Appl. Phys. 128 (4) (2020) 045101.
611 doi:10.1063/5.0009724.
612 [44] S. Plimpton, Fast parallel algotithms for short-range molecular dynamics, J. Comput. Phys. 117 (1) (1995)
613 1–19.
614 [45] A. P. Thompson, H. M. Aktulga, R. Berger, D. S. Bolintineanu, W. M. Brown, P. S. Crozier, P. J. in 't

Veld, A. Kohlmeyer, S. G. Moore, T. D. Nguyen, R. Shan, M. J. Stevens, J. Tranchida, C. Trott, S. J. Plimpton, LAMMPS - a flexible simulation tool for particle-based materials modeling at the atomic, meso, and continuum scales, Comp. Phys. Comm. 271 (2022) 108171. doi:10.1016/j.cpc.2021.108171.
[46] Soulard, L., Molecular Dynamics Study of the Micro-spallation, Eur. Phys. J. D 50 (3) (2008).
[47] L. Verlet, Computer" experiments" on classical fluids. ii. equilibrium correlation functions, Phys. Rev. 165 (1) (1968) 201.
[48] S. Nosé, A unified formulation of the constant temperature molecular dynamics methods, J. Chem. Phys. 81 (1) (1984) 511–519. doi:10.1063/1.447334.
[49] W. G. Hoover, Canonical dynamics: Equilibrium phase-space distributions, Phys. Rev. A 31 (3) (1985) 1695–1697. doi:10.1103/PhysRevA.31.1695.
[50] G. J. Martyna, D. J. Tobias, M. L. Klein, Constant pressure molecular dynamics algorithms, J. Chem. Phys. 101 (5) (1994) 4177–4189. doi:10.1063/1.467468.
[51] P. Lafourcade, C. Denoual, J.-B. Maillet, Irreversible deformation mechanisms for 1,3,5-triamino-2,4,6-trinitrobenzene single crystal through molecular dynamics simulations, J. Phys. Chem. C 122 (2018) 14954–14964.
[52] J.-M. Leyssale, G. Couégnat, S. Jouannigot, G. L. Vignoles, Mechanisms of elastic softening in highly anisotropic carbons under in-plane compression/indentation, Carbon 197 (2022) 425–434. doi:https://doi.org/10.1016/j.carbon.2022.06.063.
[53] Y. Baskin, L. Meyer, Lattice constants of graphite at low temperatures, Phys. Rev. 100 (1955) 544–544. doi:10.1103/PhysRev.100.544.
[54] C. S. G. Cousins, M. I. Heggie, Elasticity of carbon allotropes. iii. hexagonal graphite: Review of data, previous calculations, and a fit to a modified anharmonic keating model, Phys. Rev. B 67 (2003) 024109. doi:10.1103/PhysRevB.67.024109.
[55] M. Grimsditch, Shear elastic modulus of graphite, J. Phys. C: Solid State Phys. 16 (5) (1983) L143. doi:10.1088/0022-3719/16/5/002.
[56] J. B. Nelson, D. P. Riley, The thermal expansion of graphite from 15 c. to 800 c.: part i. experimental, Proc. Phys. Soc. 57 (6) (1945) 477–486. doi:10.1088/0959-5309/57/6/303.
[57] E. Kellett, B. Jackets, B. Richards, A study of the amplitude of vibration of carbon atoms in the graphite structure, Carbon 2 (2) (1964) 175–183. doi:https://doi.org/10.1016/0008-6223(64)90058-2.
[58] P. L. Walker, H. A. McKinstry, C. C. Wright, X-ray diffraction studies of a graphitized carbon - changes in interlayer spacing and binding energy with temperature., Ind. Eng. Chem. 45 (8) (1953) 1711–1715. doi:10.1021/ie50524a033.
[59] E. A. Kellett, B. P. Richards, The *c*-axis thermal expansion of carbons and graphites, J. Appl. Crystallogr. 4 (1) (1971) 1–8. doi:10.1107/S0021889871006149.
[60] B. G. A. Brito, L. Cândido, G.-Q. Hai, F. M. Peeters, Quantum effects in a free-standing graphene lattice: Path-integral against classical monte carlo simulations, Phys. Rev. B 92 (2015) 195416. doi:10.1103/PhysRevB.92.195416.
[61] C. P. Herrero, R. Ramírez, Quantum effects in graphene monolayers: Path-integral simulations, J. Chem. Phys. 145 (22) (2016) 224701. doi:10.1063/1.4971453.
[62] E. Kellett, B. Richards, The thermal expansion of graphite within the layer planes, J. Nucl. Mater. 12 (2) (1964) 184–192. doi:https://doi.org/10.1016/0022-3115(64)90139-4.
[63] A. Gamboa-Suárez, H. Y. Seuret-Hernández, J.-M. Leyssale, Mechanical properties of pristine and nanocrystalline graphene up to ultra-high temperatures, Carbon Trends 9 (2022) 100197. doi:https://doi.org/10.1016/j.cartre.2022.100197.
[64] S. I. Ranganathan, M. Ostoja-Starzewski, Universal elastic anisotropy index, Phys. Rev. Lett. 101 (2008)

055504. doi:10.1103/PhysRevLett.101.055504.
[65] C. M. Kube, Elastic anisotropy of crystals, AIP Adv. 6 (9) (2016) 095209. doi:10.1063/1.4962996.